

Numerical Simulation of Diffuse Linear Pinch

Y. Hirano* and I. Kawakami**

IPPJ-239

February 1976

Further communication about this report is to be sent to the Research Information Center, Institute of Plasma Physics, Nagoya University, Nagoya, Japan.

* Plasma Section, Electrotechnical Laboratory, Muko-odai Chyo 5-4-1, Tanashi, Tokyo, Japan.

** Department of Physics, College of Science and Technology, Nihon University, 1-8, Surugadai, Chiyoda-ku, Tokyo, Japan.

Abstract

A fully ionized plasma is considered. This plasma is assumed to be cylindrically-symmetric. The plasma is treated in hydromagnetic approximation, including electric and thermal conductivities and equipartition time. Separate temperatures are assigned to the electrons and ions.

External circuits for I_θ and I_z currents are taken into account in order to obtain the magnetic field at the boundary.

The explicit difference scheme is used for solving numerically the system of six partial differential equations.

Results of the computation are in good agreement with experimental results of ETL-TPE-1.

Comparison between the computation and snow plow model shows a good agreement in the \dot{B} and initial density dependences of the ion temperature.

Effects of the positive bias field are investigated numerically for theta pinch. It is found that the positive bias field suppresses the density concentration and reduces β of the plasma, and the ion temperature at the center has a peak about the bias field = 0.8 KG.

[1] Introduction.

Numerical treatments for one-dimensional time-dependent problems in magnetohydrodynamics are widely used for the interpretation and planning of the experiment of pinch plasma.

Several programs have been set up for this purpose, and, in general, the comparison between experiment and calculation has shown a remarkably good agreement. (1) (2) (3) (4) (5)

The purpose of this report is to describe the behavior of the pinch plasma by using the computer program developed in ETL.

Numerical model and assumptions are described in section [2]. They are almost same with those used by Hain and Roberts.

Difference methods are described in section [4] and, in this program, explicit difference scheme is used for the calculation of the quantities, such as the ion temperature, electron temperature and magnetic field.

In section [6]-(1), numerical results are compared with experimental results to demonstrate the agreement between the computation and experiment.

In section [6]-(2), numerical results are compared with the snow plow model and the character of the shock heating in the numerical calculation is discussed.

In section [6]-(3), effects of the positive bias magnetic field are investigated numerically and its influences on the ion temperature, electron temperature, density concentration and β of the plasma are discussed for the theta pinch.

[2] Assumptions and basic equations.

A fully ionized plasma is assumed to fill an infinitely long cylinder. All quantities are assumed to depend only on the radius, r . Therefore, only Z and θ components of the magnetic field are allowed. The plasma is assumed to be described as the two fluids model with quasi-neutrality, so that the stream velocity of the ions is equal to that of the electrons. The stream velocity has only one component in the r -direction.

The transport coefficients, such as the equipartition time between the ion temperature and the electron temperature, τ_{eq} , the thermal conductivities for the ions and the electrons perpendicular to the magnetic field, κ_i and κ_e , and the electric resistivity of the plasma, η , are considered. However, the ordinary viscosity of the plasma is neglected. The equipartition time is given by Spitzer⁽⁷⁾ and the thermal conductivities and the resistivity are given by Braginskii.⁽⁶⁾

Ohmic heating, ϵ_j , is confined to the electrons and the shock heating is confined to the ions.

From these assumptions, hydromagnetic equations are written as follows:

$$\frac{\partial n}{\partial t} + \frac{1}{r} \frac{\partial}{\partial r} r n u = 0, \quad (1)$$

$$\rho \left(\frac{\partial u}{\partial t} + u \frac{\partial u}{\partial r} \right) = - \frac{\partial}{\partial r} \left\{ n (T_i + Z T_e + q_i) + \frac{B_z^2}{8\pi} \right\} - \frac{B_\theta}{4\pi r} \frac{\partial}{\partial r} r B_\theta, \quad (2)$$

$$\frac{\partial T_e}{\partial t} + u \frac{\partial T_e}{\partial r} = -(\gamma-1) T_e \frac{1}{r} \frac{\partial}{\partial r} ru + (\gamma-1) \frac{\epsilon_J}{n} + \frac{\gamma-1}{n} \frac{1}{r} \frac{\partial}{\partial r} r \kappa_e \frac{\partial T_e}{\partial r} - \frac{T_e - T_i}{\tau_{eq}}, \quad (3)$$

$$\frac{\partial T_i}{\partial t} + u \frac{\partial T_i}{\partial r} = -(\gamma-1) (T_i + q_i) \frac{1}{r} \frac{\partial}{\partial r} ru + \frac{\gamma-1}{n} \frac{1}{r} \frac{\partial}{\partial r} r \kappa_i \frac{\partial T_i}{\partial r} + \frac{T_e - T_i}{\tau_{eq}}, \quad (4)$$

$$\frac{\partial B_z}{\partial t} = \frac{1}{r} \frac{\partial}{\partial r} r \left\{ \frac{c^2}{4\pi} (\eta_{\theta\theta} \frac{\partial B_z}{\partial r} - \eta_{\theta z} \frac{1}{r} \frac{\partial}{\partial r} r B_\theta) - u B_z \right\}, \quad (5)$$

$$\frac{\partial B_\theta}{\partial t} = \frac{\partial}{\partial r} \left\{ \frac{c^2}{4\pi} (\eta_{zz} \frac{1}{r} \frac{\partial}{\partial r} r B_\theta - \eta_{\theta z} \frac{\partial B_z}{\partial r}) - u B_\theta \right\}. \quad (6)$$

Here,

$$\rho = n(M_i + Zm_e) \quad ; \text{ mass density,}$$

$$\epsilon_J = \left(\frac{c}{4\pi}\right)^2 \left\{ \eta_{\theta\theta} \left(\frac{\partial B_z}{\partial r}\right)^2 - 2\eta_{\theta z} \left(\frac{\partial B_z}{\partial r}\right) \left(\frac{1}{r} \frac{\partial}{\partial r} r B_\theta\right) + \eta_{zz} \left(\frac{1}{r} \frac{\partial}{\partial r} r B_\theta\right)^2 \right\} \quad (7)$$

; input power of Joule heating,

$$q_i = M_i (a\Delta r)^2 \left(\frac{1}{r} \frac{\partial}{\partial r} ru - \left| \frac{1}{r} \frac{\partial}{\partial r} ru \right| \right) \left(\frac{1}{r} \frac{\partial}{\partial r} ru \right) \quad (8)$$

; artificial viscosity,

M_i ; ion mass,

m_e ; electron mass,

γ ; ratio of the specific heat,

η_{zz} , $\eta_{\theta\theta}$, $\eta_{\theta z}$; components of the resistivity tensor,

Δr ; mesh width.

Here, q_i is the artificial viscosity term discussed by Richtmyer.^{(8), (9)} A constant a is of order of one (In this calculation, 0.9 is used for a). This term makes it possible to compute continuously through the shock and conservation laws through the shock are guaranteed. As implied by the index i , it is assumed that the shock heating is confined to the ions, whereas the electrons behave adiabatically.

To satisfy the boundary conditions for the magnetic field self-consistently, the external circuits of the Z and θ banks are taken into account. They are shown in Figs. 1 and 2, respectively. For the Z-current, the circuit corresponding to a toroidal system is proposed, because this computation is used as an approximation of the toroidal screw pinch experiment. Therefore, the major radius of the torus, R_m , is introduced in order to calculate parameters of the Z-circuit, such as the resistance of the plasma, inductance of the plasma and inductance of the Z-coil.

It is convenient to express the parameters of the circuits in MKSA unit and the hydromagnetic equations in Gaussian unit. Under a suitable normalization, the hydromagnetic equations are connected with the circuit equations easily.

Eqs. (9), (10), (11) and (12) represent the Z-circuit and Eqs. (13), (14) and (15) represent the θ -circuit.

$$(L_{Tz} + L_{cz}) \frac{dI_{ez}}{dt} - L_{cz} \frac{dI_{pz}}{dt} + R_{Tz} I_{ez} + \frac{Q_z}{C_z} = 0 \quad (9)$$

$$L_{pz} \frac{dI_{pz}}{dt} - L_{cz} \frac{dI_{ez}}{dt} + R_{pi} I_{pz} + \frac{\partial \phi_{pz}}{\partial t} = 0 \quad (10)$$

$$\frac{dQ_z}{dt} = I_{ez} \quad (11)$$

$$\phi_{pz} = 2\pi R_m \int_0^{r_{wall}} B_\theta dr \quad (12)$$

$$(L_{T\theta} + L_{c\theta}) \frac{dI_\theta}{dt} + R_{T\theta} I_\theta + \frac{Q_\theta}{C_\theta} + \frac{\partial \phi_{p\theta}}{\partial t} = 0 \quad (13)$$

$$\frac{dQ_\theta}{dt} = I_\theta \quad (14)$$

$$\phi_{p\theta} = 2\pi \int_0^{r_{wall}} B_z r dr \quad (15)$$

$L_{c\theta}$; leakage inductance between the θ -coil and plasma.

Here, I_{ez} , I_{pz} and I_θ are the currents flowing in the Z-coil, plasma and θ -coil, respectively. The currents I_{pz} and I_θ are proportional to the θ and Z components of the magnetic field at the wall, $B_{\theta wall}$ and $B_{z wall}$, respectively. ϕ_{pz} and $\phi_{p\theta}$ are total magnetic fluxes of the θ and Z direction in the discharge tube, respectively. Q_θ and Q_z are electric charges contained in the θ and Z capacitors, respectively. The effective total resistance of the plasma, R_{pi} , is defined as follows,

$$R_{pi} = \frac{4\pi^2 R_m^2}{I_{pz}^2} \int_0^{r_{wall}} \eta_{zz} j_z^2 r dr, \quad (16)$$

where r_{wall} is the radius of the discharge tube. Eq. (16) means that the macroscopic Joule heating energy, $R_{\text{pi}} I_{\text{pz}}^2$, is equivalent to the integral of the microscopic Joule heating energy, $\eta_{\text{zz}} j_z^2$.

[3] Normarization and Lagrangian description of the equations.

For convenience, the equations are normarized by suitable factors. Normarization factors are listed in Appendix [I].

It is known that the Lagrangian description of the hydro-magnetic equations improves the numerical stability in the difference forms.⁽⁹⁾ Therefore, Eqs. (1)~(7), are transformed from the Eulerian coordinates, (R, t) , to the Lagrangian coordinates, (x, t) . The relations between (R, t) and (x, t) are given by,

$$\frac{\partial R}{\partial x} = \frac{1}{nR} \quad ,$$

$$\frac{\partial R}{\partial t} = v \quad ,$$

$$t = t \quad ,$$

in normarized forms.

Normarized forms of Eqs. (1)~(7) written by the Lagrangian coordinates are listed in Appendix [II].

The transport coefficients and other constants in normarized forms are listed in Appendix [III].

Normarized equations for the external circuits are written in Appendix [IV]. In those equations, $b_{\theta e}$, $b_{\theta w}$ and b_{zw} correspond to the currents flowing in the Z-coil, plasma and θ -coil,

respectively, and b_{zw} and $b_{\theta w}$ are the normalized Z and θ components of the magnetic field at the wall, respectively.

[4] Difference scheme for the computation

In order to solve the equations in the central difference form, the half integral mesh is used for the velocity and the integral mesh is used for other quantities with respect to space and time. This method improves the numerical stability of the difference equations.⁽⁹⁾

However, the artificial viscosity term in the equation for velocity, Eq. (A-2), can not be written in the central difference form, because $(\frac{1}{R} \frac{\partial}{\partial R} RV)^2$ is included in this term. Therefore, the following iteration for this term is introduced.

$$i) \quad (v_{j+1/2}^k)^s = \frac{1}{2} ((v_{j+1/2}^{k+1/2})^s + v_{j+1/2}^{k-1/2})$$

$$ii) \quad (\text{div } \vec{V})_j^{k,s} = \frac{1}{R_j} \frac{R_{j+1/2} (v_{j+1/2}^k)^s - R_{j-1/2} (v_{j-1/2}^k)^s}{\Delta R}$$

$$iii) \quad (q_j^k)^s = q_0 \cdot ((\text{div } \vec{V})_j^{k,s} - |(\text{div } \vec{V})_j^{k,s}|) (\text{div } \vec{V})_j^{k,s}$$

$$iv) \quad (v_{j+1/2}^{k+1/2})^{s+1} = v_{j+1/2}^{k-1/2} - \frac{\Delta t}{\Delta x_{j+1/2}^k} ((q_{j+1}^k)^s - (q_j^k)^s) - \frac{\Delta t}{\Delta x_{j+1/2}^k} G_{j+1/2}^k$$

(17)

Here,

$$\begin{aligned}
G_{j+1/2}^k &= R_{j+1/2} (C_1 \cdot (P_{j+1}^k - P_j^k) \\
&\quad + C_2 (b_{zj+1}^k + b_{zj}^k) (b_{zj+1}^k - b_{zj}^k)) \\
&\quad + C_2 (b_{\theta j+1}^k + b_{\theta j}^k) (R_{j+1} b_{\theta j+1}^k - R_j b_{\theta j}^k) ,
\end{aligned}$$

$$P_j^k = N_j^k (Z^T e_j^k + T_{ij}^k)$$

and

$$\Delta x_{j+1/2}^k = \frac{1}{2} (N_{j+1}^k + N_j^k) \cdot R_{j+1/2} \cdot \Delta R.$$

(The index s indicates the number of times of the iteration and, j and k indicate a certain space and time point, respectively.)

For $s=0$, $v_{j+1/2}^{k-1/2}$ is substituted for $(v_{j+1/2}^{k+1/2})^{s=0}$ and then $(v_{j+1/2}^{k+1/2})^{s=1}$ is calculated by the equations i), ii), iii) and iv). Next, $(v_{j+1/2}^{k+1/2})^{s=2}$ is calculated from $(v_{j+1/2}^{k+1/2})^{s=1}$ by the same way and so on.

This iteration is repeated only for three times in this program because the recognizable difference is not observed for $s \geq 3$.

The values of the Lagrangian space points at $t=t^{k+1/2}$ and $t=t^{k+1}$ are obtained from $v^{k+1/2}$ as follows,

$$x_j^{k+1} = R_j + \frac{1}{2} (v_{j+1/2}^{k+1/2} + v_{j-1/2}^{k+1/2}) \cdot \Delta t$$

$$x_{j+1/2}^{k+1/2} = R_{j+1/2} + \frac{1}{2} (v_{j+1/2}^{k+1/2} + v_{j+1/2}^{k-1/2}) \cdot \Delta t .$$

Here, R_j and $R_{j+1/2}$ are the uniform space points and are given at $t=0$.

The stability criterion for the explicit difference scheme of the hydromagnetic equations is given by,⁽⁹⁾

$$\Delta t \leq \Delta t_{\text{mu}} = \frac{\Delta x}{\sqrt{C_s^2 + V_A^2}} \quad (18)$$

Here,

$$C_s^2 = \frac{Z T_e}{M_i} \quad ; \text{ sound velocity,}$$

$$V_A^2 = \frac{B^2}{4\pi n M_i} \quad ; \text{ Alfvén velocity,}$$

and

$$\Delta x = nr\Delta r \quad ; \text{ mesh width of the Lagrangian coordinates.}$$

In the ordinary case, V_A is much greater than C_s and Δt_{mu} is written as follows approximately,

$$\Delta t_{\text{mu}} = \frac{nr\Delta r}{V_A} = \sqrt{4\pi M_i} \cdot \frac{n^{3/2}\Delta r}{B}$$

Because of the low density and strong magnetic field near the wall, Δt_{mu} has the smallest value at the wall. Therefore, it is sufficient to consider Δt_{mu} only at the wall and the maximum time step in the normalized form is written as follows,

$$\Delta t_{\text{mu}} = \frac{N_{\text{wall}} R_{\text{wall}} \Delta R}{\sqrt{C_{s0}^2 + V_{A0}^2 \frac{b_{\text{wall}}^2}{N_{\text{wall}}}}} \quad (19)$$

where,

$$C_{s0} = \frac{Z T_0}{M_i V_0^2} \quad \text{and} \quad V_{A0} = \frac{B_0^2}{4\pi M_i n_0 V_0^2}$$

Another restriction required for the stability is that the Lagrangian space points must not cross each other.⁽⁹⁾ When the stability condition, $\Delta t \leq \Delta t_{\text{mu}}$, is violated or the crossing of the Lagrangian space points occurs, $\Delta t/2$ is taken as a new time step and the velocity at the step $t=t^{k+1/4}$ is calculated.

When the stability conditions are satisfied, the velocity on the uniform space point $R_{j+1/2}$ is calculated from $v_{j+1/2}^{k+1/2}$. The value of $v_{j+1/2}^{k+1/2}$ obtained from Eq.(17) is the value on the Lagrangian space point $X_{j+1/2}^{k+1/2}$. Namely, $v_{j+1/2}^{k+1/2}$ means $v^{k+1/2}(X_{j+1/2}^{k+1/2})$. The Lagrangian space points move with the plasma, so that the space points are rare in regions where the density is low. However, the magnetic field varies even in the low density regions. Moreover, the boundary condition in which the plasma comes off the wall is used, (Section [5]). This would change the number of the Lagrangian space points. In order to avoid these difficulties the velocity on the uniform space points, $v^{k+1/2}(R_{j+1/2})$, is calculated from $v^{k+1/2}(X_{j+1/2}^{k+1/2})$ at each step by the linear interpolation. By this method, the velocity is always obtained on the uniform space points at the end of the each step and it is possible to regard $R_{j+1/2}$ as a new position of the Lagrangian space point, $X_{j+1/2}$ at $t=t^{k+1/2}$. This scheme is called modified Lagrangian scheme and is illustrated in Fig.3.

The field quantities, T_e^{k+1} , T_i^{k+1} , b_θ^{k+1} and b_z^{k+1} are calculated by the explicit difference equations derived from Eq.(A-3) ~ Eq.(A-6), respectively. The density N^{k+1} is calculated by the difference equation derived from the equation of the density conservation,

Eq. (A-1).

A type of those equations is given by,

$$F_j^{k+1} = F_j^k + \frac{\Delta t}{\Delta x_j^k} \left(\frac{A_{j+1/2}^k}{\Delta x_{j+1/2}^k} (F_{j+1}^k - F_j^k) - \frac{A_{j-1/2}^k}{\Delta x_{j-1/2}^k} (F_j^k - F_{j-1}^k) \right) + \Delta t B_j^k F_j^k + \Delta t C_j^k \quad (20)$$

Here, F represents a certain field quantity and, A_j^k , B_j^k and C_j^k are the functions of $v_{j+1/2}^{k+1/2}$ and some field quantities.

The stability condition for Eq. (20) is given by,⁽⁹⁾

$$\Delta t \leq \Delta t_{mf} = \text{Minimum}_{2 \leq j \leq J_{\max} - 1} \left(\left| \frac{1}{2 \left(\frac{A_{j+1/2}^k}{\Delta x_{j+1/2}^k} + \frac{A_{j-1/2}^k}{\Delta x_{j-1/2}^k} \right) - B_j^k} \right|, \left| \frac{F_j^k}{C_j^k} \right| \right)$$

If the time step, Δt , is greater than Δt_{mf} , then, $\Delta t/2$ is taken as a new time step and the calculations for the field quantities are repeated until the stability conditions is satisfied.

Next, according to the modified Lagrangian scheme, the field quantities on the uniform space point, $F_j^{k+1}(R_j)$, are calculated from $F_j^{k+1} = F_j^{k+1}(X_j^{k+1})$.

If Δt is smaller than $(2/5)\Delta t_M$, then, $2\Delta t$ is taken as a new time step for the calculation of the next step $t=t^{k+2}$, where Δt_M is given as follows,

$$\Delta t_M = \text{Minimum} (\Delta t_{mf}, \Delta t_{\mu}).$$

Difference equations for the θ and Z circuits are written in Appendix [V]. In those equations, the half integral mesh with respect to time is used for q_θ and q_z , and the integral mesh is used for other quantities.

In the explicit difference scheme, it is possible to obtain $\phi_{p\theta}^{k+1}$ and ϕ_{pz}^{k+1} without any iteration. To prove this, $\phi_{p\theta}^{k+1}$ is taken as an example.

From the definition, Eq.(A-14), $\phi_{p\theta}^{k+1}$ is given by,

$$\phi_{p\theta}^{k+1} = \int_0^{R_{J_{\max}-1}} b_z^{k+1} R dR + \int_{R_{J_{\max}-1}}^{R_{\text{wall}}} b_z^{k+1} R dR, \quad (21)$$

where J_{\max} indicates the space point at the wall, so that $R_{J_{\max}}$ means R_{wall} and $R_{J_{\max}-1}$ does the first space point from the wall. By the explicit difference equation for b_z , the value of b_z^{k+1} is obtained on all space points except the boundary, $R=R_{\text{wall}}$. Therefore, the first term of the right hand side of Eq.(21) can be calculated by the numerical integration. The second term is approximated to,

$$\int_{R_{J_{\max}-1}}^{R_{\text{wall}}} b_z^{k+1} R dR \approx \frac{\Delta R}{2} [R_{\text{wall}} \cdot b_{zw}^{k+1} + R_{J_{\max}-1} \cdot b_{zJ_{\max}-1}^{k+1}] .$$

Therefore, $\phi_{p\theta}^{k+1}$ is given by,

$$\phi_{p\theta}^{k+1} = S^{k+1} + P \cdot b_{zw}^{k+1}, \quad (22)$$

where,

$$S^{k+1} = \int_0^{R_{Jmax-1}} b_z^{k+1} R dR + \frac{\Delta R}{2} R_{Jmax-1} \cdot b_{zJmax-1}^{k+1}$$

and

$$P = \frac{\Delta R}{2} R_{wall} .$$

Substituting Eq.(22) into Eq.(A-15), b_{zw}^{k+1} can be solved as follows,

$$b_{zw} = \frac{\{ (1_{T\theta} + 1_{c\theta} - \frac{\Delta t}{2} R_{T\theta}) b_{zw}^k - \Delta t \frac{q_{\theta}^{k+1/2}}{c_{\theta}} - S^{k+1} + \phi_{p\theta}^k \}}{(1_{T\theta} + 1_{c\theta} + \frac{\Delta t}{2} R_{T\theta} + P)} \quad (23)$$

The same procedure is applied to the Z circuit and $b_{\theta w}^{k+1}$ is obtained by the straightforward calculation.

[5] Boundary conditions.

At the center of the discharge tube, the symmetry around $r=0$ is required and following conditions are imposed;

$$u = 0 ,$$

$$\frac{\partial T_e}{\partial r} = \frac{\partial T_i}{\partial r} = 0 ,$$

$$\frac{\partial B_z}{\partial r} = \frac{\partial r B_{\theta}}{\partial r} = 0 .$$

No boundary condition is required for the density because the density is calculated from the conservation of the density around $r=0$.

On the wall, the following conditions are assumed;

- i) $u=0$; at $j=J_{\max} + \frac{1}{2}$, i.e., $r=r_{\text{wall}} + \frac{\Delta r}{2}$,
- ii) T_e, T_i ; fixed to the initial values,
- iii) $B_z = B_{z\text{wall}}$,

$$B_\theta = B_{\theta\text{wall}}.$$

Here, $B_{z\text{wall}}$ and $B_{\theta\text{wall}}$ are obtained from the external circuits, respectively.

The condition for the velocity, i), means that the flux of the plasma, $\frac{1}{2}u_{J_{\max}-1/2} \cdot n_{\text{wall}}$ is introduced at the wall, where, n_{wall} is the plasma density at the wall.

In order to obtain the boundary condition for the density, it is assumed that the plasma interacts with the wall strongly and is neutralized immediately at the wall. Therefore, the density is allowed only to decrease at the wall until it reaches to a certain minimum value, n_{\min} . Thus, n_{wall} is given by,

$$n_{\text{wall}}^{k+1} = \text{Max.} (\text{Min.} (n_{\text{wall}}^{k+1}, n_{\text{wall}}^k), n_{\min}),$$

where, index k indicates the step $t=t^k$. In the dilute plasma region which is surrounding the hot dense main plasma column, the density and the electron temperature depend on n_{\min} and the current

distribution in the plasma depends on the distribution of the electron temperature. The value of n_{\min} is to be determined by the recycling of the plasma on the wall. The intensity of the plasma flux coming off the wall is also to be determined by it. However, the mechanism of the recycling of the plasma is very complicated and is not clear. Therefore, it is impossible to determine the value of n_{\min} selfconsistently. In this program, n_{\min} is given artificially so as to obtain the reasonable electron temperature in the dilute plasma region, comparing with the experimental value.

The boundary condition for the temperatures, \bar{T} , is also the result of the strong interaction between the plasma and wall. Because the energy exchange between the plasma and wall is sufficiently large under this interaction and the heat capacity of the wall is much larger than that of the plasma.

[6] Results of computations

(1) Comparison with the experiment.

Numerical results are compared with the experiment of ETL-TPE-1. (10), (11)

Following initial conditions are used for the numerical calculation and experiment.

° initial density, n_{in} ; $1.5 \times 10^{15}/\text{cm}^3$

° charging voltage

Θ -Bank ; 20 kV ($B_{z\max} \approx 10$ kG)

Z-Bank ; 20 kV ($B_{\theta\max} \approx 2.1$ kG)

° rising time of the magnetic field.

B_z ; 2.9 μ s

B_θ ; 2.5 μ s

° gas specy ; Helium

The initial temperature of the plasma is not measured in the experiment and it is assumed to be 1 eV in the computation.

Figs. 4 and 5 show the time evolutions of $B_{z\text{wall}}$ and $B_{\theta\text{wall}}$, respectively. Reactions of the radial oscillation of the plasma to $B_{z\text{wall}}$ and $B_{\theta\text{wall}}$ are observed in Figs. 4 and 5.

Fig. 6 shows the time evolution of B_z at the center of the discharge tube, B_{zC} , and the maximum compression time of the plasma. The small black circle, •, indicates the experimental value of B_{zC} measured by the magnetic probe and the solid line does the numerical one. The double circle, ⊙, and large black circle, ●, indicate the maximum compression time measured by the intensity of the bremsstrahlung and the streak photograph, respectively.

The period of the radial oscillation of the plasma and the value of B_{zC} are in good agreement with experimental results at the early stage of the discharge. Fig. 7 shows the diamagnetic signal. The broken line indicates the experimental value and solid line does the numerical one. The periods of the oscillation of the numerical value and experimental one show a good

agreement at the early stage. However, the magnitude of the numerical value is greater than the experimental one by a factor 2.5. In particular, the difference of the first peak means that the penetration of the magnetic field into the plasma is faster in the experiment than in the computation. Fig. 8 shows the radial profiles of B_z and B_θ , and Fig. 9 shows the radial profiles of T_e and n_e . In Figs. 8 and 9, the values of B_z , B_θ , T_e and n_e are in fairly good agreement with the experimental values.

(2) Comparison with the snow plow model.

As described in section [2], the artificial viscosity is necessary for the numerical calculation of the shock by the difference method, although the physical meaning of the artificial viscosity is not clear. The ions are heated by the artificial viscosity in the numerical calculation.

In this section, the artificial viscosity is examined for the ion heating by comparing the numerical results with the snow plow model. For simplicity, only the θ -pinch is considered.

For the deuterium plasma and $r_{\text{wall}}=5$ cm, the energy into the plasma by the θ discharge is estimated by the following equation in the snow plow model.⁽¹²⁾

$$W = 28.2 \frac{(\dot{B}/10^9)}{(n_{\text{in}}/10^{15})^{1/2}} \text{ eV} \quad (24)$$

where, n_{in} and \dot{B} are the initial density and the rising rate of the magnetic field, respectively.

When the equipartition time between the ions and electrons is much longer than the pinch time, the ion temperature is almost equal to W . On the other hand, when the equipartition time is much shorter than the pinch time, the ion temperature is same with the electron temperature and is equal to $W/2$. In Fig.10, the n_{in} dependence of $\bar{T}_{icenter}$ is shown. The black circle represents the numerical value and the solid line does the snow plow model. $\bar{T}_{icenter}$ is the mean value of the ion temperature at the center ($r=0$) and is defined as follows,

$$\bar{T}_{icenter} = \frac{1}{t_2 - t_1} \int_{t_1}^{t_2} T_{icenter} dt,$$

where t_1 is the first pinch time and t_2 is the second one.

In Fig.10, $\bar{T}_{icenter}$ is given approximately as follows,

$$\bar{T}_{icenter} = 66 (n_{in}/10^{15})^{-0.6} \text{ eV} \quad (25)$$

In Fig.11, the \dot{B} dependence of $\bar{T}_{icenter}$ is shown. In this figure $\bar{T}_{icenter}$ is given approximately as follows,

$$\bar{T}_{icenter} = 9.3 \left(\frac{\dot{B}}{10^9} \right)^{1.2} \text{ eV.} \quad (26)$$

In Fig.12, the B_{max} dependence of $\bar{T}_{icenter}$ is shown, where the frequency of the θ -circuit, f_0 , is fixed to constant ($f_0=86.2$ kHz) and only the charging voltage is varied. In Fig.12, $\bar{T}_{icenter}$ is given approximately as follows,

$$\bar{T}_{\text{icenter}} = 2.3 \left(\frac{B_{\text{max}}}{10^3} \right)^{1.5}. \quad (27)$$

Since \dot{B} is equal to $2\pi f_0 B_{\text{max}}$, the \dot{B} dependence of \bar{T}_{icenter} , Eq. (26), is modified as follows,

$$\begin{aligned} \bar{T}_{\text{icenter}} &= 9.3 \left(\frac{2\pi f_0 B_{\text{max}}}{10^9} \right)^{1.2} \\ &= 4.5 \left(\frac{B_{\text{max}}}{10^3} \right)^{1.2} \end{aligned} \quad (28)$$

Then, the B_{max} dependence of \bar{T}_{icenter} , Eq. (27), is written as follows,

$$\bar{T}_{\text{icenter}} = 4.5 \left(\frac{B_{\text{max}}}{10^3} \right)^{1.2} 0.52 \left(\frac{B_{\text{max}}}{10^3} \right)^{0.3}. \quad (29)$$

Comparing Eq. (28) and Eq. (29), it is found that \bar{T}_{icenter} is essentially dependent on $B_{\text{max}}^{0.3}$. This B_{max} dependence of the ion temperature is a notable difference between the numerical calculation and the snow plow model.

It is shown that T_i is proportional to $B_{\text{max}}^{1.4}$ in the modified snow plow model, ⁽¹³⁾ in which the adiabatic compression by the magnetic field is taken into account after the shock heating. It was also reported that T_i was proportional to $B_{\text{max}}^{1.7}$ in the experiment of ETL-TPE-1 ⁽¹¹⁾ and to $E_{\theta} B_{\text{max}} \propto B_{\text{max}}^{1.5}$ in the experiment of Cylar IV in Los Alamos. ⁽¹⁴⁾ The equation (27) is in good agreement with these results.

From Eqs. (25), (26) and (27), Eq. (30) is derived.

$$\bar{T}_{\text{icenter}} = 4.85 \frac{(\dot{B}/10^9)^{1.2} (B_{\text{max}}/10^3)^{0.3}}{(n_{\text{in}} / 10^{15})^{0.6}} \quad (30)$$

Eq. (30) approximately agrees with the snow plow model over the ranges of $\dot{B}=10^9 \sim 10^{10}$ G/S, $n_{\text{in}}=5 \times 10^{14} \sim 5 \times 10^{15}/\text{cm}^3$ and $B_{\text{max}}=5 \sim 25$ kG. For $B_{\text{max}}=10$ kG, \bar{T}_{icenter} is given by

$$\bar{T}_{\text{icenter}} = 8.4 (\dot{B}/10^9)^{1.2} / (n_{\text{in}} / 10^{15})^{0.6} \quad (31)$$

in the numerical calculation and given by

$$\bar{T}_{\text{icenter}} = 14.1 (\dot{B}/10^9) / (n_{\text{in}}/10^{15})^{0.5} \quad (32)$$

in the snow plow model. ($T_i=T_e=W/2$ is assumed.) Then, good agreement is obtained.

(3) Effects of the positive bias field.

It is known that the β of the plasma can not exceed a certain critical value, β_c , in the toroidal equilibrium of the high β tokamak configuration.⁽¹⁵⁾ However it is difficult to maintain a stable equilibrium in the experiment of the toroidal screw pinch,⁽¹¹⁾ because β exceeds the critical value by the over concentration of the plasma density at the center of the discharge tube. It is known in the experiment that the density concentration is able to be controlled by the positive bias magnetic field in the toroidal direction, B_0 .⁽¹¹⁾

In this section, the effect of the bias field is investigated numerically for the θ pinch and the B_0 dependences of the ion tem-

perature, density concentration and β are described. The result obtained from the numerical calculation is, of course, the cylindrical one, whereas the experiment is the toroidal one. However, in the experiment of the large aspect ratio like ETL-TPE-1, the toroidal effect is sufficiently small for the density concentration and heating of the plasma at the early stage of the discharge.

Numerical results are shown in Figs. 13 and 14. In Fig. 13 T_{ic} , T_{ec} , n_c and τ_{eqc} are the ion temperature, electron temperature, density and equipartition time at the center of the discharge tube, respectively. In Fig. 14, \bar{T}_i , \bar{T}_e , $\bar{\beta}$ and K_{pm} are the mean ion temperature, mean electron temperature, mean β and maximum kinetic energy of the plasma, respectively, and are defined as follows,

$$\bar{T}_i = \frac{\int_0^{r_{wall}} n T_i r dr}{\int_0^{r_{wall}} n r dr}$$

$$\bar{T}_e = \frac{\int_0^{r_{wall}} n T_e r dr}{\int_0^{r_{wall}} n r dr}$$

$$\bar{\beta} = \frac{\frac{2}{r_{wall}^2} \int_0^{r_{wall}} n (T_i + Z T_e) r dr}{(B_{\theta wall}^2 + B_{z wall}^2) / 8\pi}$$

and

$$K_{pm} = \text{Maximum } (K_p(t)), \quad 0 \leq t \leq 3\mu s$$

where,

$$K_p = 2\pi M_i \int_0^{r_{wall}} n u^2 r dr.$$

An example of the time evolution of the kinetic energy of the plasma, K_p , is shown in Fig. 15.

Since the maximum value of the magnetic field is near the 8th peak of the radial oscillation, the values of T_{ic} , T_{ec} , n_c , τ_{eqc} , \bar{T}_i , \bar{T}_e and $\bar{\beta}$ at that time are shown in Figs. 13 and 14.

In Fig. 13, it is found that the bias field is effective on the suppression of the density concentration. In Fig. 14, the B_0 dependence of K_{pm} shows that the speed of the shock decreases as B_0 increases. However, the effect of the bias field is not so great on the speed of the shock as on the density concentration and it is found from Figs. 13 and 14 that the reduction of $\bar{\beta}$ by the bias field is the consequence of the suppression of the density concentration.

An interesting effect of the bias field appears in the behavior of the ion temperature at the center, T_{ic} , and is shown in Fig. 13. Namely, according as the bias field increases, T_{ic} does not vary monotonously but has a peak about $B_0=0.8$ kG. The behavior of T_{ic} is interpreted as the results of following two effects.

① In Fig. 13, it is shown that, for $B_0 \approx 1$ kG, n_c decreases by a factor 0.5 and T_{ec} decreases by a factor 0.8 in comparison with the case of $B_0=0$. Therefore, τ_{eqc} is relatively long and the only small portion of the ion energy is transferred to the electrons. Consequently, T_{ic} is higher than that for $B_0=0$.

This effect does not appear in the region where B_0 is greater than 1.8 kG, because T_{ec} is lower than 50 eV and τ_{eqc} is shorter

than the pinch time.

② In Figs. 13 and 14, it is shown that the positive bias field is more effective on the suppression of the density concentration than on the reduction of the shock speed, in the region where B_0 is about 1 kG. Therefore, input energy per unit density increases at the center as the bias field increases. Consequently, T_{ic} is relatively higher for $B_0 \approx 1$ kG than that for $B_0 = 0$.

However, in region where B_0 is greater than about 1.5 kG, the reduction of the shock speed by the bias field is dominant and T_{ic} is lower than the case of no bias field.

[7] Conclusion

A numerical scheme for computing the dynamics of the pinch plasma is set up in the cylindrical symmetry.

The comparison between the computation and experiment of ETL-TPE-1 shows a fairly good agreement.

A formula for the estimation of the ion temperature in the θ pinch is obtained from the computation. In this formula, the ion temperature is proportional to $B^{1.2}/n_{in}^{0.6}$. This shows a fairly good agreement with the snow plow model. The B_{max} dependence of the ion temperature is in good agreement with the experiments and modified snow plow model, which include the effect of the adiabatic compression by the magnetic field.

In the θ pinch, the concentration of the plasma density by the hydromagnetic shock is suppressed by applying the positive bias field. This suppression of the density concentration results

in the reduction of β of the plasma. Although the mean ion temperature decreases monotonously as the bias field increases, the ion temperature at the center has a peak about the bias field = 0.8 kG. This behavior of the ion temperature can be interpreted as a result of the less concentration of the density at the center. The effects of the positive bias field for the ion temperature at the center and β of the plasma are favorable to the confinement of the toroidal screw pinch, because it is possible to reduce β without lowering the ion temperature.

Acknowledgement

The authors would like to thank Dr. S. Kiyama, Dr. Y. Maejima, Dr. K. Ogawa, Dr. H. Ashida and other members of the Plasma Section of Electrotechnical Laboratory for their helpful discussions. The authors are also grateful to Dr. T. Tamaru and Dr. M. Kito for their encouragement.

FIGURE CAPTIONS

Fig. 1. Current circuit for the Z-current.

L_{TZ} ; total inductance of the capacitor,
cable and collector plate.

R_{TZ} ; total resistance of the capacitor,
cable and collector plate.

L_{CZ} ; inductance of the Z-coil.

$M=L_{CZ}$; mutual inductance between the Z-coil and plasma.

L_{pz} ; external inductance of the plasma.

C_z ; capacitance of the Z-bank.

Fig. 2. Current circuit for the θ -current.

$L_{T\theta}$; total inductance of the capacitor,
cable and collector plate.

$R_{T\theta}$; total resistance of the capacitor,
cable and collector plate.

C_θ ; capacitance of the θ -bank.

Fig. 3. Illustration of the modified Lagrangian scheme.

Fig. 4. Time evolution of B_{zwall} .

Fig. 5. Time evolution of $B_{\theta wall}$.

Fig. 6. Time evolution of B_z at $r=0$ and the maximum compression times.

Fig. 7. Diamagnetic signal of the plasma.

Fig. 8. Radial profiles of B_z and B_θ .

Fig. 9. Radial profiles of the electron temperature and electron density.

Fig. 10. n_{in} dependence of $\bar{T}_{icenter}$.

$$B_{max} = 10 \text{ kG}$$

$$\dot{B} = 5.46 \times 10^9 \text{ G/S}$$

Fig. 11. \dot{B} dependence of $\bar{T}_{icenter}$.

$$B_{max} = 10 \text{ kG}$$

$$n_{in} = 10^{15}/\text{cm}^3$$

Fig. 12. B_{max} dependence of $\bar{T}_{icenter}$.

$$f_0 = 86.2 \text{ kHz}$$

$$n_{in} = 10^{15}/\text{cm}^3$$

Fig. 13. Bias dependences of the density, ion temperature, electron temperature and equipartition time at $r=0$.

Fig. 14. Bias dependences of the mean ion temperature, mean electron temperature, mean β value and maximum kinetic energy of the plasma in the discharge tube.

Fig. 15. Time evolution of the kinetic energy of the plasma in the discharge tube.

In Figs. 13, 14 and 15, following parameters are used.

$$r_{wall} \quad ; \quad 5 \text{ cm}$$

$$B_{max} \quad ; \quad 10 \text{ kG} \quad (V_{\theta} = 20 \text{ k volt})$$

$$\dot{B} \quad ; \quad 5.46 \times 10^9 \text{ G/S}$$

$$n_{in} \quad ; \quad 10^{15}/\text{cm}^3$$

$$\text{Gas} \quad ; \quad \text{deuterium}$$

Initial temperature of the plasma

$$; \quad 1 \text{ eV}$$

REFERENCES

- (1) K. Hain, G. Hain, K. V. Roberts, S. J. Roberts,
W. Köppendörfer : Z. Naturforsch, vol. 15a, 1039 (1960)
- (2) T. A. Oliphant : LAMS-2944, TID-4500 (23rd Ed.) (1973)
- (3) F. Hoffmann : Lausanne Rep. LRP-46/71 (1971)
- (4) I. Kawakami : IPPJ-DT-23 (1970), in Japanese.
- (5) Y. Hirano, S. Kiyama, T. Shimoda, K. Ogawa : Bul. Electrotech.
Lab. vol. 38, Nos. 3~5 156 (1974) in Japanese.
- (6) S. I. Braginskii : Rev. of Plasma Phys. vol. 1, 205
- (7) L. Spitzer : Theory of Fully Ionized Gases, Interscience
Publ. New York (1956)
- (8) J. Von Neumann, R. D. Richtmyer : J. Applied Phys., vol. 21,
March, 91 (1950)
- (9) R. D. Richtmyer and K. W. Morton : Difference Methods for
Initial Value Problems, Interscience Publ., New York (1967)
- (10) K. Ogawa, et al. : Bul. Electrotech. Lab., vol. 38, Nos.
3~5, 91 (1974)
- (11) K. Ogawa, et al. : IAEA-CN-33/E9-4 Tokyo (1974)
- (12) L. A. Artsimovich : Controlled Thermonuclear Reactions,
Gordon and Breach Science Publ., New York
- (13) S. Kiyama : private communication
- (14) R. F. Gribble, W. E. Quinn, R. F. Siemon : Phys. of Fluids,
vol. 14, No. 9, 2042 (1971)
- (15) V. D. Shafranov : Rev. of Plasma Phys., vol. 2, 103

Appendix I

Normalization factors.

For magnetohydrodynamic equations;

density	n_0	$10^{15}/\text{cm}^3$	$n=n_0 N$
length (radius)	r_0	1 cm	$r=r_0 R$
time	t_0	10^{-6} sec	$t=t_0 t$
velocity	$V_0=r_0/t_0$	10^6 cm/sec	$u=V_0 V$
magnetic field	B_0	10^3 gauss	$B=B_0 b$
temperature	T_0	1.60206×10^{-12} erg	$T=T_0 T$

For Z-circuit;

current	$I_{0z} = 2\pi r_{\text{wall}}^* B_0^* / \mu_0$	$I_{ez}^* = I_{0z} b_{\theta e}$
		$I_{pz}^* = I_{0z} b_{\theta w}$
inductance	$L_{0z} = \mu_0 r_0^{*2} / r_{\text{wall}}^*$	$L^* = L_{0z} l$
flux	$\Phi_{0z} = 2\pi r_0^{*2} B_0^*$	$\Phi_{pz}^* = \Phi_{0z} \phi_{pz}$
charge	$Q_{0z} = 2\pi r_{\text{wall}}^* B_0^* t_0 / \mu_0$	$Q_z^* = Q_{0z} q_z$
capacitance	$C_{0z} = r_{\text{wall}}^* t_0^2 / (\mu_0 r_0^{*2})$	$C_z^* = C_{0z} c_z$
resistance	$R_{0z} = \mu_0 r_0^{*2} / (r_{\text{wall}}^* t_0)$	$R^* = R_{0z} R$

For theta-circuit;

current	$I_{0\theta} = 2\pi R_m^* B_0^* / \mu_0$	$I_{\theta}^* = I_{0\theta} b_{zw}$
inductance	$L_{0\theta} = \mu_0 r_0^{*2} / R_m^*$	$L^* = L_{0\theta} l$
flux	$\Phi_{0\theta} = 2\pi r_0^{*2} B_0^*$	$\Phi_{p\theta}^* = \Phi_{0\theta} \phi_{p\theta}$
charge	$Q_{0\theta} = 2\pi R_m^* B_0^* t_0 / \mu_0$	$Q_{\theta}^* = Q_{0\theta} q_{\theta}$
capacitance	$C_{0\theta} = R_m^* t_0^2 / (\mu_0 r_0^{*2})$	$C_{\theta}^* = C_{0\theta} c_{\theta}$
resistance	$R_{0\theta} = \mu_0 r_0^{*2} / (R_m^* t_0)$	$R^* = R_{0\theta} R$

* indicates that the values are expressed in MKSA unit.

Other values are expressed in Gaussian unit.

($r_0^* = 0.01$ m, $B_0^* = 0.1$ wb/m², $\mu_0 = 4\pi \times 10^{-7}$)

Appendix II

Normalized hydromagnetic equations.

$$\frac{\partial N}{\partial t} + N \operatorname{div} \vec{V} = 0 \quad (\text{A-1})$$

$$\frac{\partial V}{\partial t} = -C_1 R \frac{\partial}{\partial x} N (z T_e + T_i + q_i) - C_2 R \frac{\partial}{\partial x} b_z^2 - 2C_2 b_\theta \frac{\partial}{\partial x} R b_\theta \quad (\text{A-2})$$

$$\frac{\partial T_e}{\partial t} = -(\gamma-1) T_e \operatorname{div} \vec{V} + \frac{\partial}{\partial x} \kappa_e \frac{\partial T_e}{\partial x} + \bar{\epsilon}_J - (T_e - T_i) \cdot t_{eq}^{-1} \quad (\text{A-3})$$

$$\frac{\partial T_i}{\partial t} = -(\gamma-1) (T_i + q_i) \operatorname{div} \vec{V} + \frac{\partial}{\partial x} \bar{\kappa}_i \frac{\partial T_i}{\partial x} - z (T_i - T_e) \cdot t_{eq}^{-1} \quad (\text{A-4})$$

$$\frac{\partial b_z}{\partial t} = N \frac{\partial}{\partial x} (\bar{\eta}_{\theta\theta} \frac{\partial b_z}{\partial x} - \bar{\eta}_{\theta z} \frac{\partial}{\partial x} R b_\theta) - b_z \operatorname{div} \vec{V} \quad (\text{A-5})$$

$$\frac{\partial b_\theta}{\partial t} = NR \frac{\partial}{\partial x} (\bar{\eta}_{zz} \frac{\partial}{\partial x} R b_\theta - \bar{\eta}_{\theta z} \frac{\partial b_z}{\partial x}) - NR b_\theta \frac{\partial V}{\partial x} \quad (\text{A-6})$$

$$\operatorname{div} \vec{V} = N \frac{\partial}{\partial x} RV \quad (\text{A-7})$$

Appendix III

Normalized forms of the transport coefficients and other constants.

N_{mesh} ; number of mesh points.

$$R_{\text{wall}} = r_{\text{wall}} / r_0$$

$$\Delta R = R_{\text{wall}} / N_{\text{mesh}}$$

$$m_A = M_i + Zm_e$$

$$C_1 = T_0 / (r_0^2 m_A)$$

$$C_2 = B_0^2 / (8\pi m_A v_0^2 n_0)$$

$$q_i = q_0 (\text{div } \vec{V} - |\text{div } \vec{V}|) \text{div } \vec{V}$$

$$q_0 = m_A v_0^2 (a \Delta R)^2 / (2T_0), \quad a=0.9$$

$$\bar{\epsilon}_J = \epsilon_0 \left\{ \bar{n}_{\theta\theta} \left(\frac{\partial b_z}{\partial x} \right)^2 - 2\bar{n}_{\theta z} \left(\frac{\partial b_z}{\partial x} \right) \left(\frac{\partial}{\partial x} R b_\theta \right) + \bar{n}_{zz} \left(\frac{\partial}{\partial x} R b_\theta \right)^2 \right\}$$

$$\epsilon_0 = (\gamma-1) B_0^2 / (4\pi n_0 T_0 Z)$$

$$\bar{\kappa}_e = \kappa_{e0} N^2 R^2 T_e (\gamma'_1 x_e^2 + \gamma'_0) t_e / \Delta_e$$

$$\kappa_{e0} = (\gamma-1) T_0 / (m_e v_0^2)$$

$$\bar{\kappa}_i = \kappa_{i0} N^2 R^2 T_i (2Y^2 + 2.645) t_i / \Delta_i$$

$$\kappa_{i0} = (\gamma-1) T_0 / (M_i v_0^2)$$

$$t_{\text{eq}} = \frac{2m_e}{m_A} \frac{1}{t_e}$$

$$\bar{n}_{zz} = n_0 \frac{1}{t_e} \left(1 + \delta\eta \frac{b_\theta^2}{b^2} \right)$$

$$\bar{n}_{\theta z} = -n_0 \frac{1}{t_e} \delta\eta \frac{b_\theta b_{zR}}{b^2}$$

$$\bar{n}_{\theta\theta} = n_0 \frac{1}{t_e} (1 + \delta\eta \frac{b_z^2}{b^2}) R^2$$

$$\delta\eta = \frac{1}{\alpha_0} (1 - \frac{\alpha'_1 x_e^2 + \alpha'_0}{\Delta_e}) - 1$$

$$\Delta_e = x_e^4 + \delta_1 x_e^2 + \delta_0$$

$$x_e = x_{0e} b t_e$$

$$x_{0e} = eB_0 t_0 / (m_e c)$$

$$\Delta_i = y^4 + 2.70y^2 + 0.677$$

$$y = y_0 b t_i$$

$$y_0 = ZeB_0 t_0 / (cM_i)$$

$$b = (b_z^2 + b_\theta^2)^{1/2}$$

$$t_e = \tau_e / t_0 = t_{e0} \frac{T_e^{3/2}}{N \ln \Lambda}$$

$$t_{e0} = \frac{3\sqrt{m_e} T_0^{3/2}}{4\sqrt{2\pi} e^4 Z^2 n_0 t_0}$$

$$t_i = \tau_i / t_0 = t_{i0} \frac{T_i^{3/2}}{N \ln \Lambda}$$

$$t_{i0} = \frac{3\sqrt{m_i} T_0^{3/2}}{4\sqrt{\pi} e^4 Z^4 n_0 t_0}$$

$$\ln \Lambda = \ln \frac{\sqrt{3m_e} c T_0}{137\sqrt{\pi} e^3 \sqrt{n_0}} - 1.5 \ln Z + \ln T_e - 0.5 \ln N$$

for $T_e \geq 50$ eV

$$= \ln \frac{3T_0^{3/2}}{2\sqrt{\pi} e^3 \sqrt{n_0}} - 1.5 \ln Z + 1.5 \ln T_e - 0.5 \ln N$$

for $T_e \leq 50$ eV

The values of the constants α_0 , α'_1 , α'_0 , γ'_1 , γ'_0 , δ'_1 and δ'_0 are given by Braginskii.⁽⁶⁾

Appendix IV

Normarized forms of the circuit equations.

For Z-circuit ($B_{\theta wall}$) ;

$$(l_{Tz} + l_{cz}) \frac{db_{\theta e}}{dt} + R_{Tz} b_{\theta e} + \frac{q_z}{c_z} - l_{cz} \frac{db_{\theta w}}{dt} = 0 . \quad (A-8)$$

$$l_{pz} \frac{db_{\theta w}}{dt} + R_{pi} b_{\theta w} - l_{cz} \frac{db_{\theta e}}{dt} + \frac{\partial \phi_{pz}}{\partial t} = 0 . \quad (A-9)$$

$$\frac{dq_z}{dt} = b_{\theta e} . \quad (A-10)$$

$$\phi_{pz} = \frac{R_m}{r_0} \int_0^{R_{wall}} b_{\theta} dR . \quad (A-11)$$

$$R_{pi} = R_{p0} \frac{1}{b_{\theta w}^2} \int_0^{R_{wall}} \frac{\bar{\eta}_{zz}}{N} \frac{1}{R} \left(\frac{\partial R b_{\theta}}{\partial R} \right)^2 dR .$$

$$R_{p0} = 9 \times 10^{11} \cdot \frac{4\pi R_m r_0^2}{c^2 r_{wall}^2 t_0} .$$

For θ -circuit ($B_{z wall}$) ;

$$(l_{T\theta} + l_{c\theta}) \frac{db_{z w}}{dt} + R_{T\theta} b_{z w} + \frac{q_{\theta}}{c_{\theta}} + \frac{\partial \phi_{p\theta}}{\partial t} = 0 . \quad (A-12)$$

$$\frac{dq_{\theta}}{dt} = b_{z w} . \quad (A-13)$$

$$\phi_{p\theta} = \int_0^{R_{wall}} b_z R dR . \quad (A-14)$$

Appendix V

The difference equations for theta and Z circuits.

For theta circuit;

$$\begin{aligned} & (l_{T\theta} + l_{c\theta}) (b_{zw}^{k+1} - b_{zw}^k) + \frac{\Delta t}{2} R_{T\theta} (b_{zw}^{k+1} + b_{zw}^k) \\ & + \Delta t \frac{q_{\theta}^{k+1/2}}{c_{\theta}} + (\phi_{p\theta}^{k+1} - \phi_{p\theta}^k) = 0, \end{aligned} \quad (A-15)$$

$$q_{\theta}^{k+1/2} - q_{\theta}^{k-1/2} = \Delta t b_{zw}^k, \quad (A-16)$$

For Z circuit ;

$$\begin{aligned} & (l_{Tz} + l_{cz}) (b_{\theta e}^{k+1} - b_{\theta e}^k) + \frac{\Delta t}{2} R_{Tz} (b_{\theta e}^{k+1} + b_{\theta e}^k) + \Delta t \frac{q_z^{k+1/2}}{c_z} \\ & - l_{cz} (b_{zw}^{k+1} - b_{zw}^k) = 0, \end{aligned} \quad (A-17)$$

$$\begin{aligned} & l_{pz} (b_{\theta w}^{k+1} - b_{\theta w}^k) + \frac{\Delta t}{2} R_{pi} (b_{\theta w}^{k+1} + b_{\theta w}^k) - l_{cz} (b_{\theta e}^{k+1} - b_{\theta e}^k) \\ & - (\phi_{pz}^{k+1} - \phi_{pz}^k) = 0, \end{aligned} \quad (A-18)$$

$$q_z^{k+1/2} - q_z^{k-1/2} = \Delta t b_{\theta e}^k \quad (A-19)$$

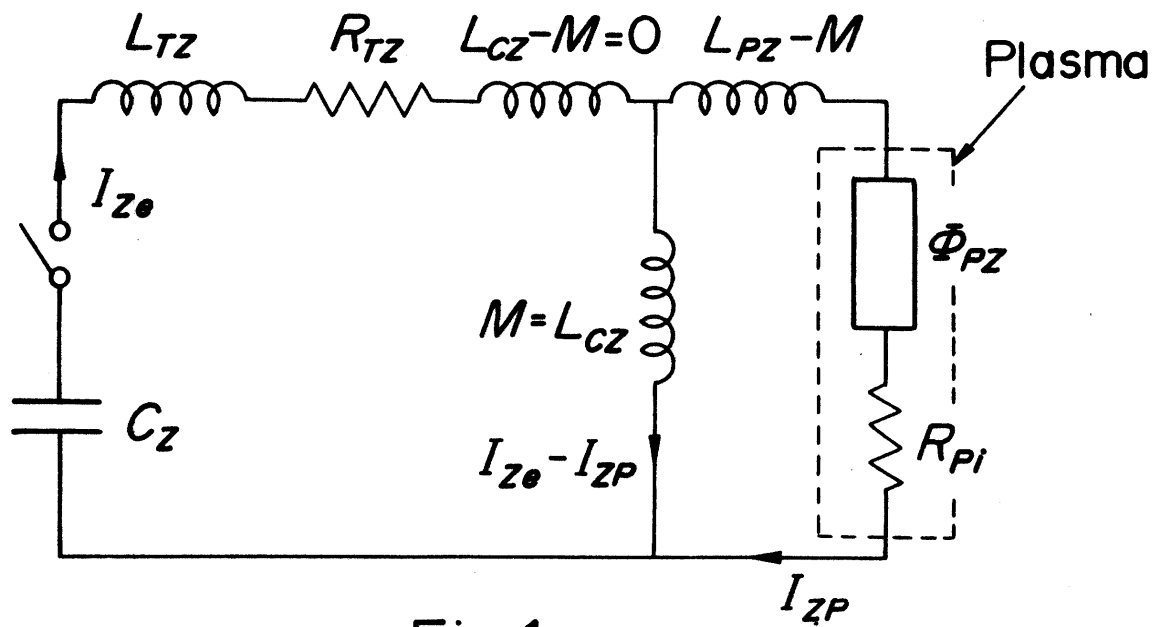


Fig. 1

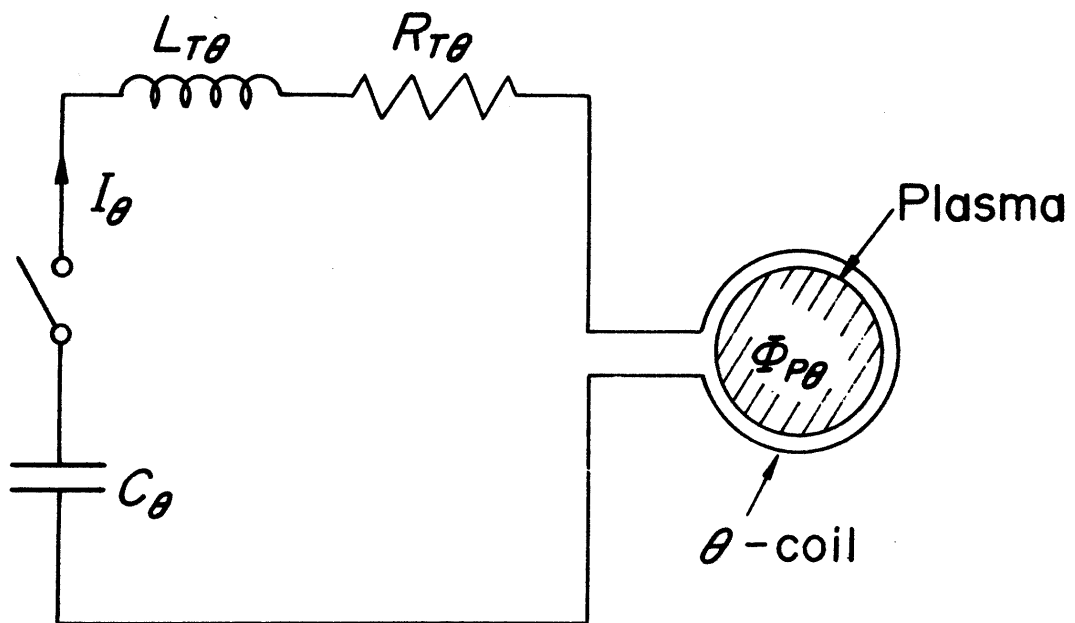


Fig. 2

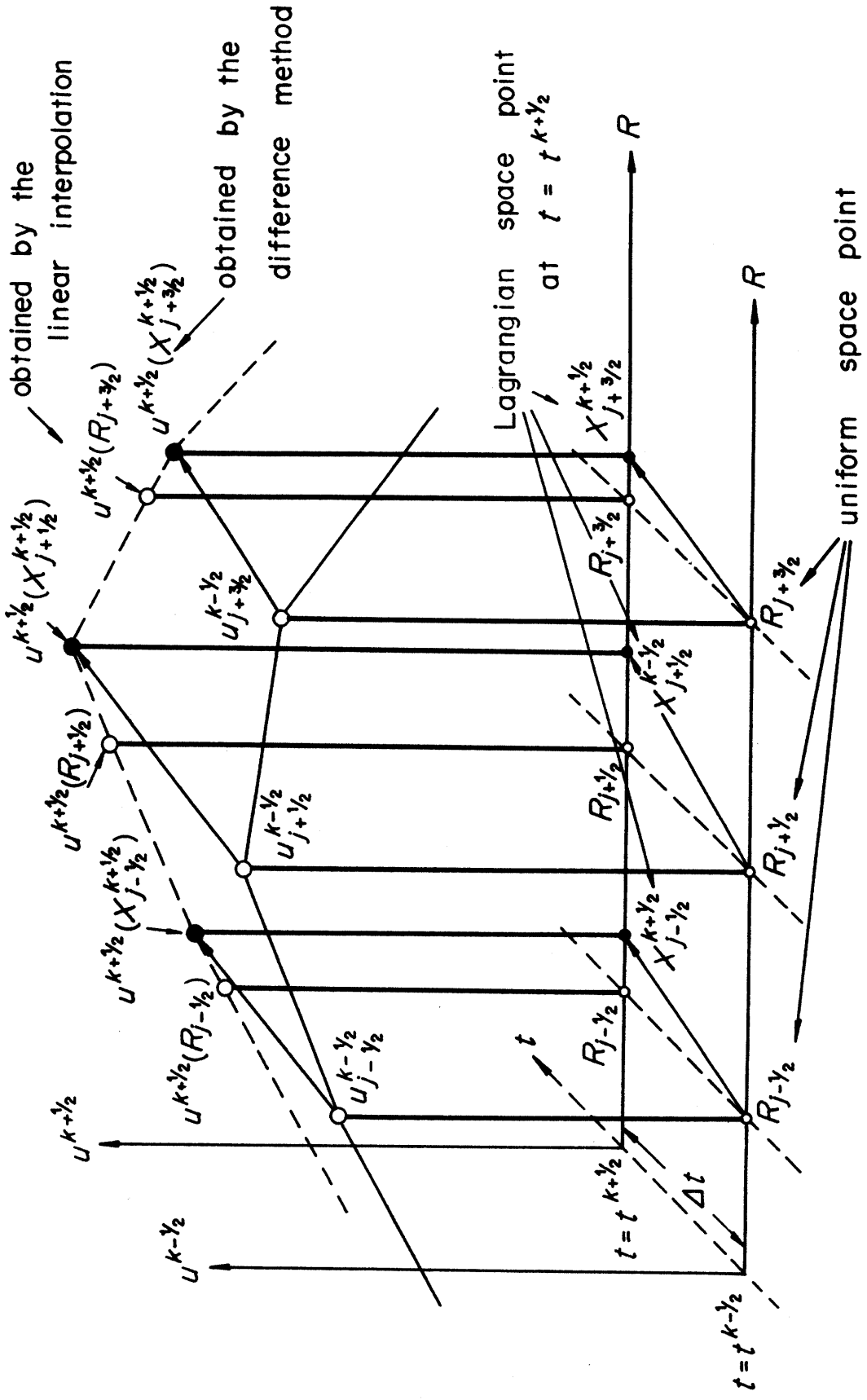


Fig. 3

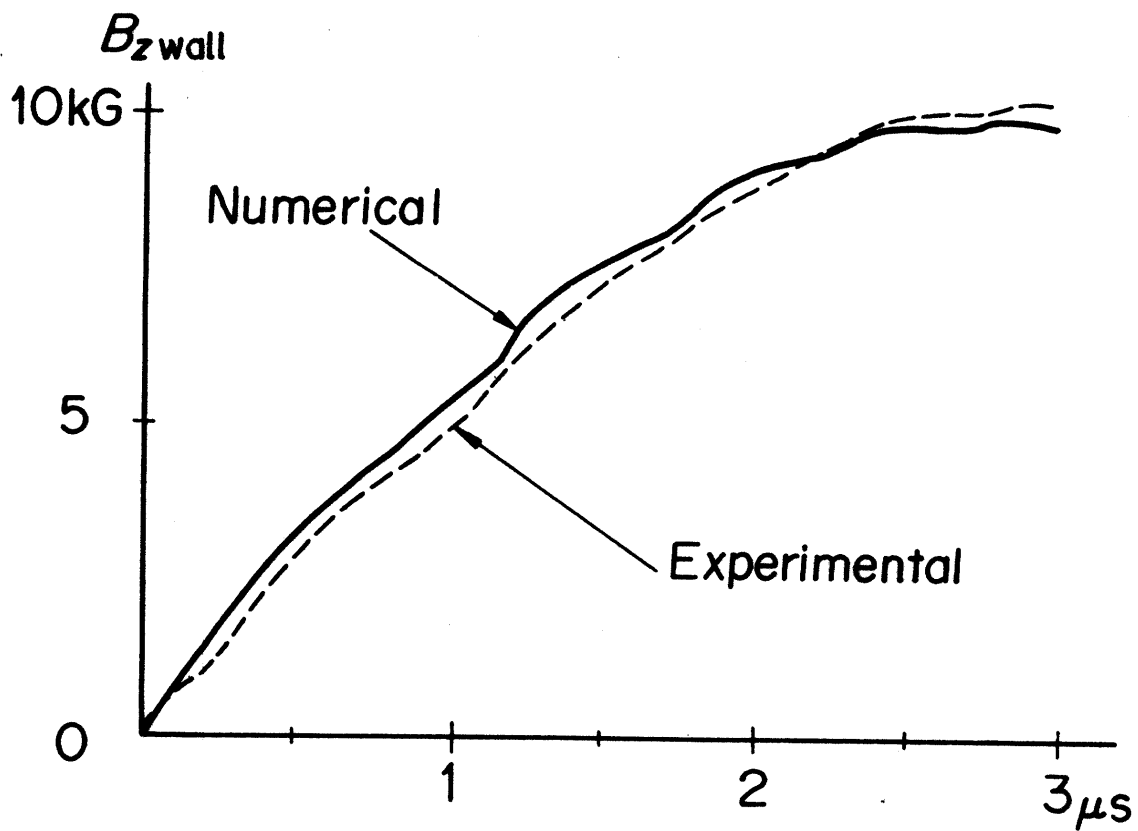


Fig. 4

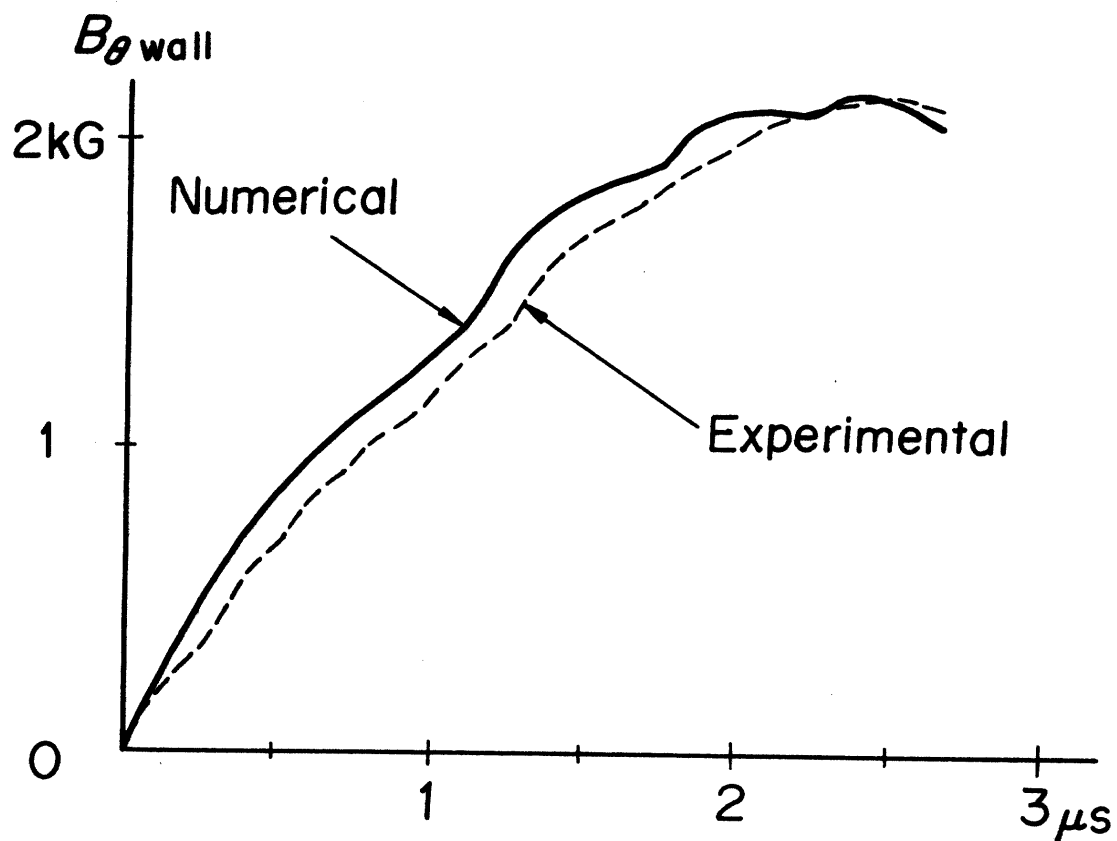


Fig. 5

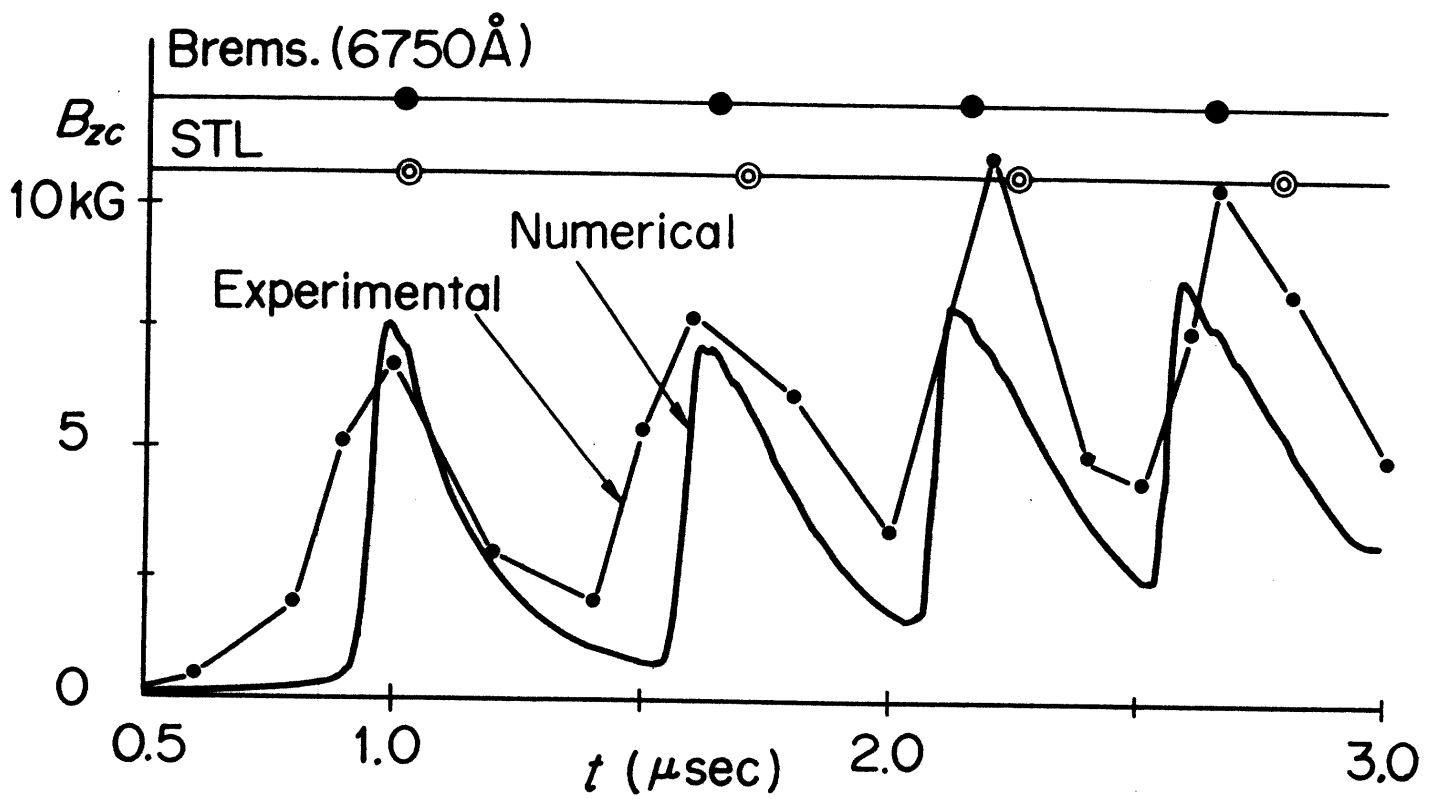


Fig. 6

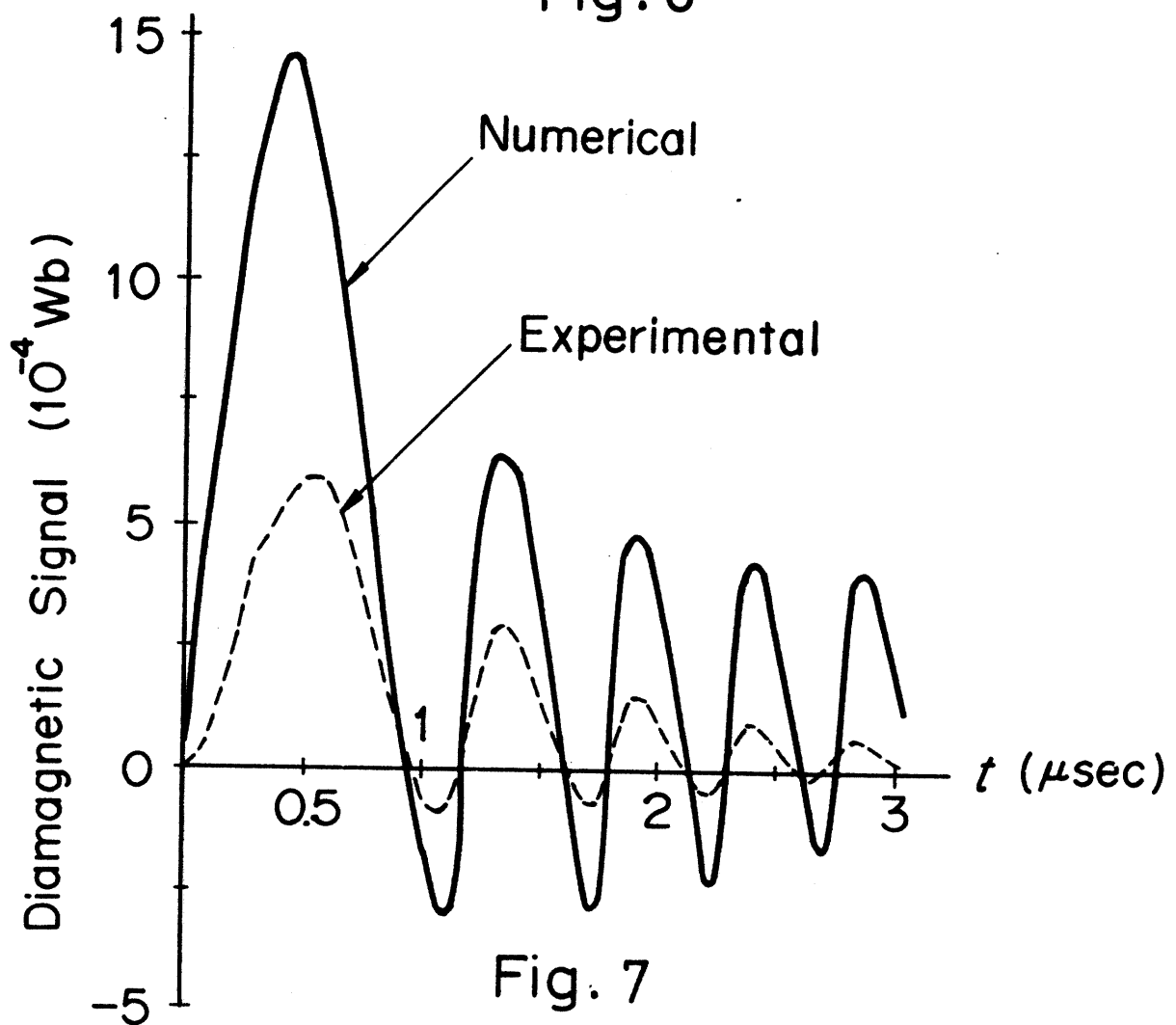


Fig. 7

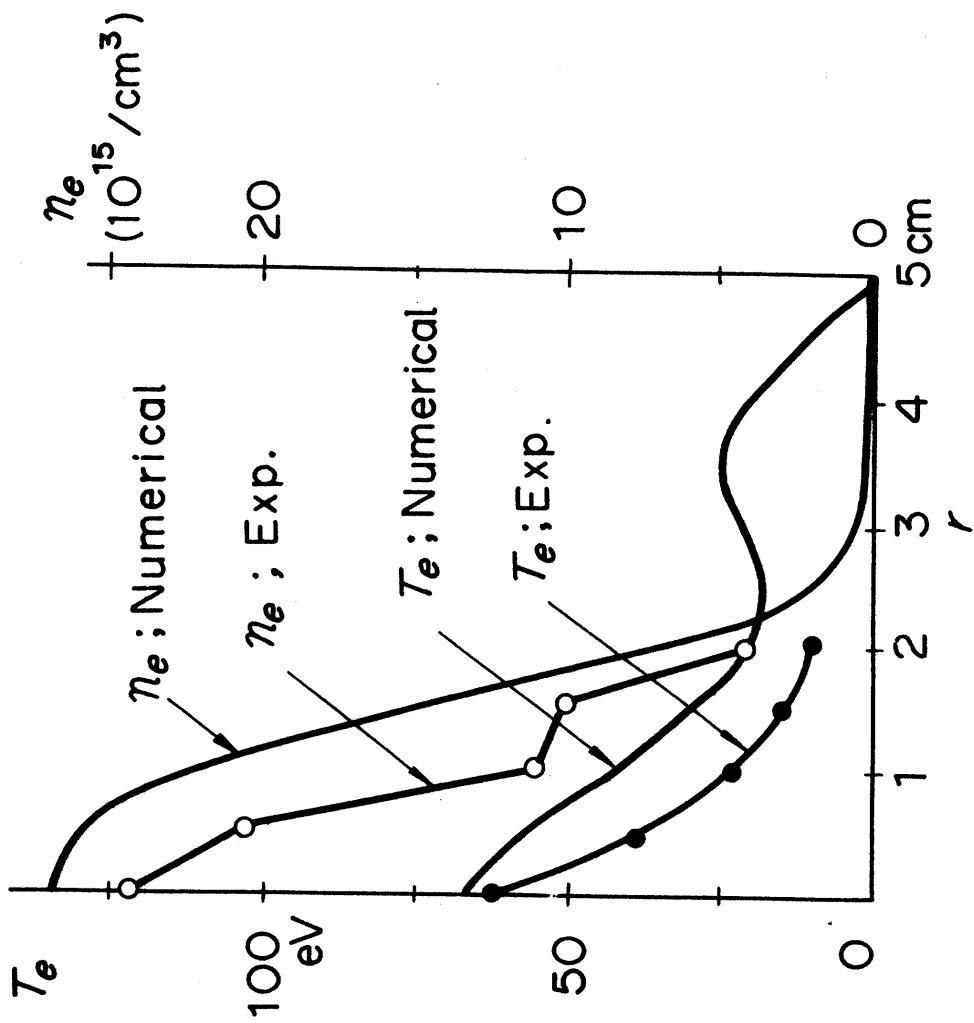


Fig. 9

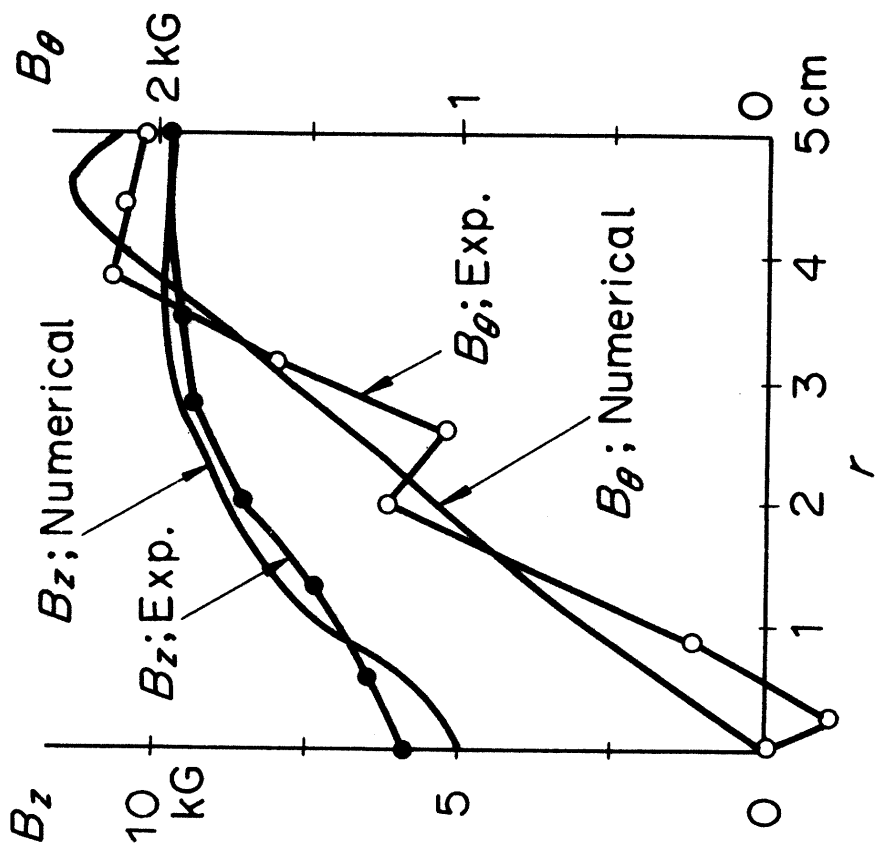


Fig. 8

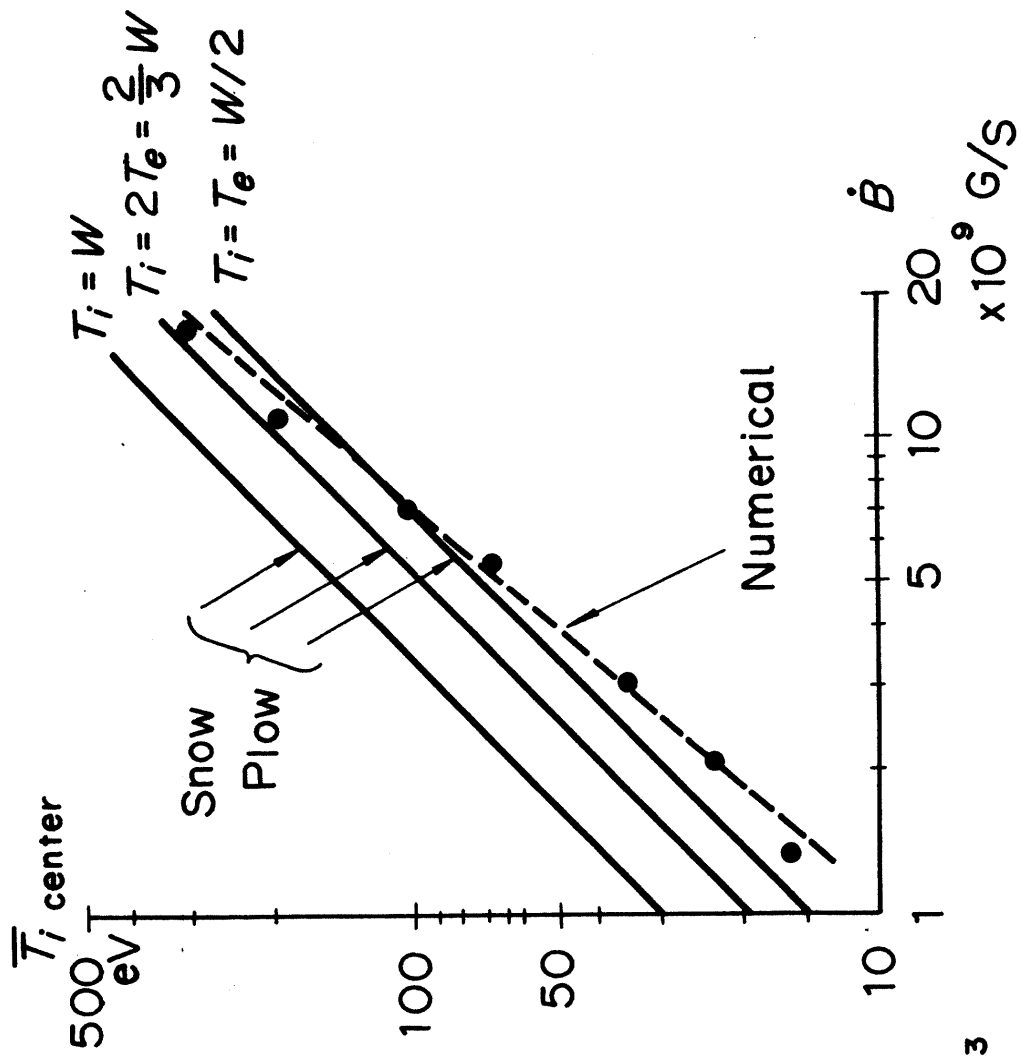


Fig.11

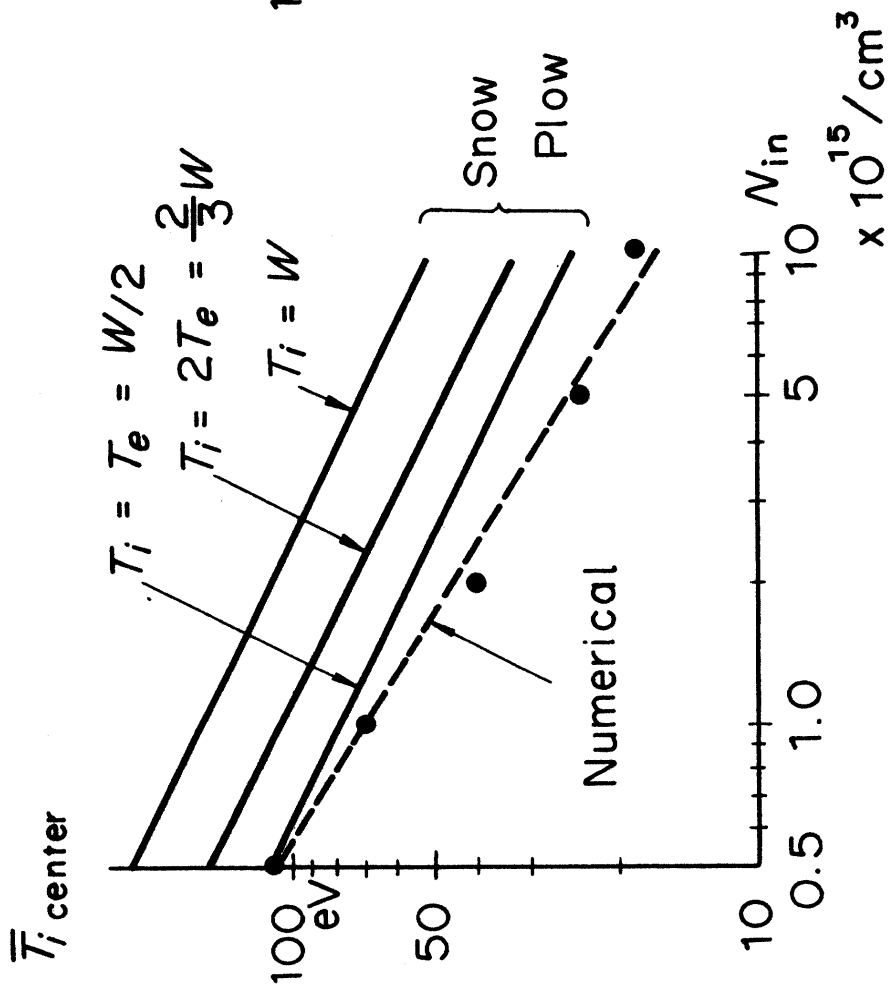


Fig.10

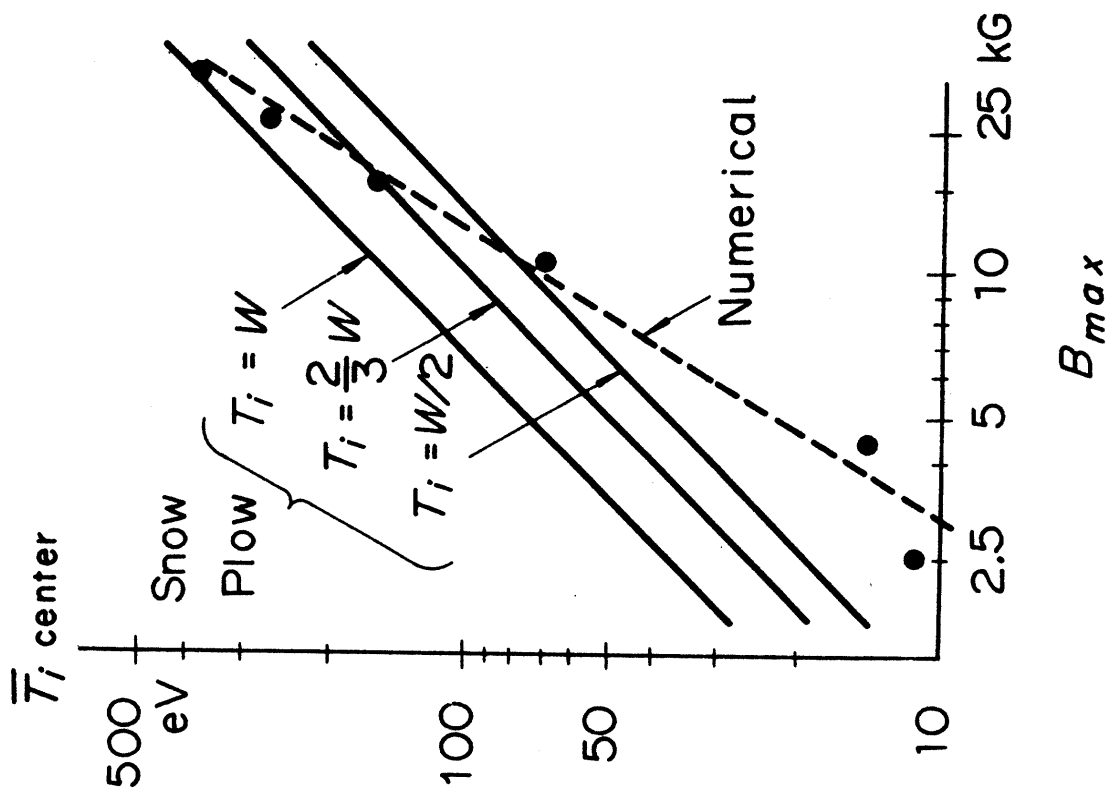


Fig.12

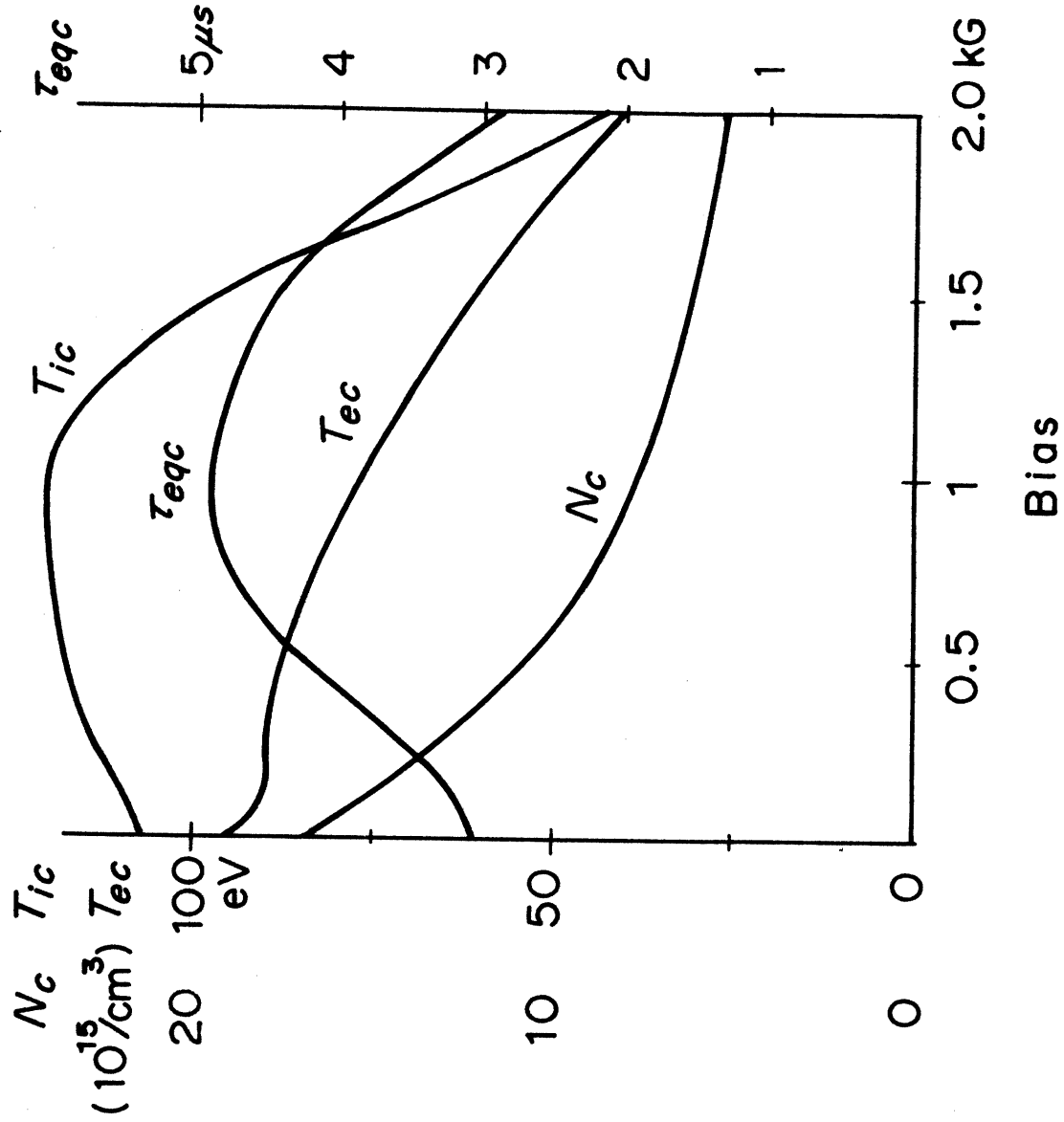


Fig.13

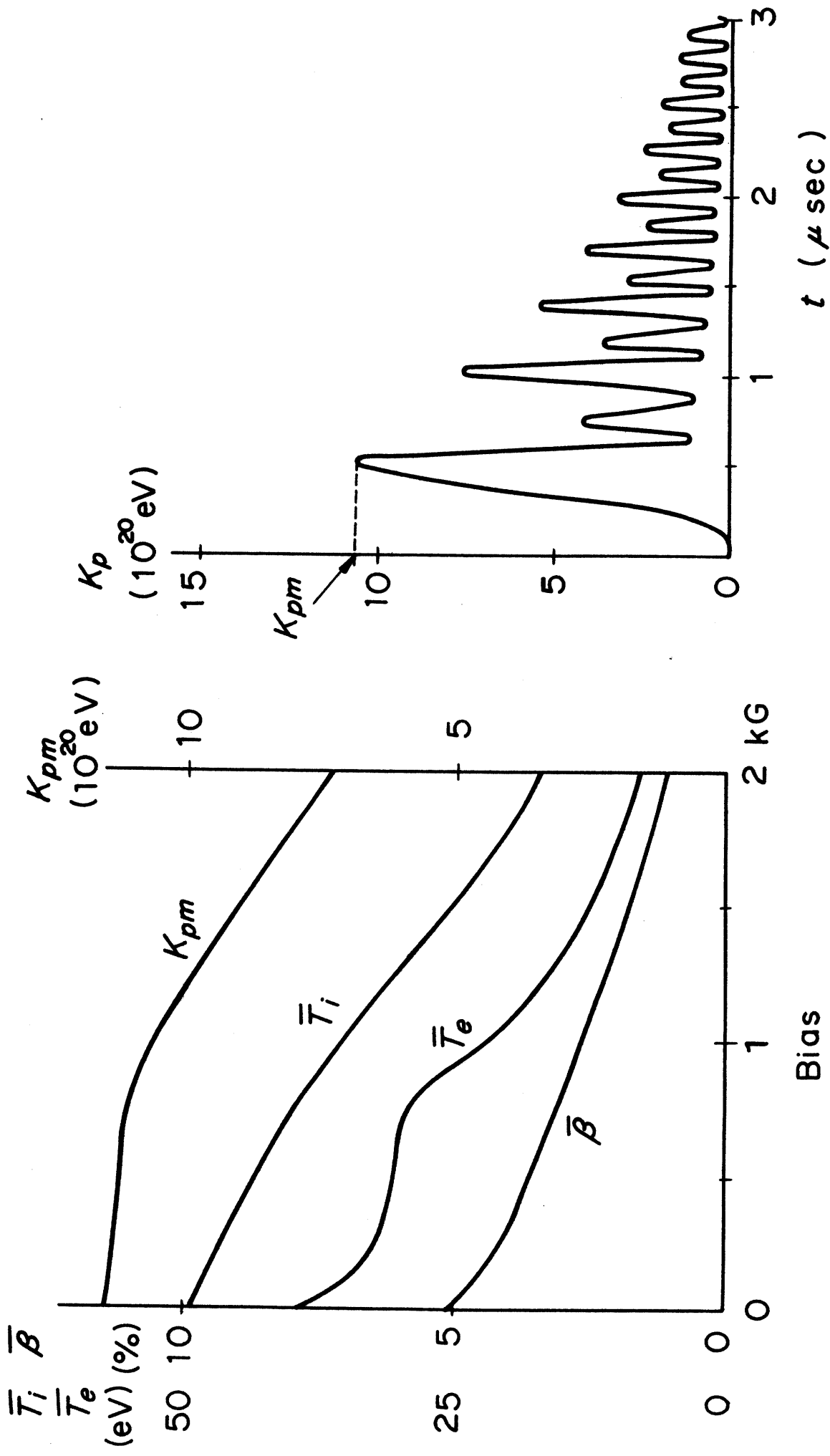


Fig.14

Fig.15